Faradays Discussions
Cite this: *Faraday Discuss.*, 2023, **247**, 45

PAPER

Electrochemical hydrogen isotope exchange of amines controlled by alternating current frequency†

Nibedita Behera, ‡ Disni Gunasekera, ‡ Jyoti P. Mahajan, Joseph Frimpong, Zhen-Fei Liu and Long Luo *

Received 18th February 2023, Accepted 13th March 2023
DOI: 10.1039/d3fd00044c

Here, we report an electrochemical protocol for hydrogen isotope exchange (HIE) at α-C(sp^3)–H amine sites. Tetrahydroisoquinoline and pyrrolidine are selected as two model substrates because of their different proton transfer (PT) and hydrogen atom transfer (HAT) kinetics at the α-C(sp^3)–H amine sites, which are utilized to control the HIE reaction outcome at different applied alternating current (AC) frequencies. We found the highest deuterium incorporation for tetrahydroisoquinolines at 0 Hz (*i.e.*, under direct current (DC) electrolysis conditions) and pyrrolidines at 0.5 Hz. Analysis of the product distribution and D isotope incorporation at different frequencies reveals that the HIE of tetrahydroisoquinolines is limited by its slow HAT, whereas the HIE of pyrrolidines is limited by the overoxidation of its α-amino radical intermediates. The AC-frequency-dependent HIE of amines can be potentially used to achieve selective labeling of α-amine sites in one drug molecule, which will significantly impact the pharmaceutical industry.

Introduction

Hydrogen isotope (D or T)-labeled organic molecules are essential to support drug discovery and development in the pharmaceutical industry. For example, deuterated compounds are used as stable isotope-labeled internal standards for quantification purposes in all "omics" fields, taking advantage of the mass shift arising from the substitution of H by D in a given molecule.[1–4] Furthermore, due to the primary kinetic isotope effect, D incorporation at specific positions of a bioactive molecule can potentially decrease its metabolism rate and/or prevent the formation of toxic metabolites, leading to the emergence of deuterated drugs.[5,6] The labeling efficiency and selectivity requirements vary with the application.[7] In the first application discussed above, multiple incorporations of

Department of Chemistry, Wayne State University, Detroit, Michigan 48202, USA. E-mail: long.luo@wayne.edu
† Electronic supplementary information (ESI) available. See DOI: https://doi.org/10.1039/d3fd00044c
‡ Equally contributing (first) authors.

hydrogen isotopes are often required. In the last one, selective hydrogen labeling at a specific position is more critical than multiple-site labeling.

Among all hydrogen isotope labeling methods, hydrogen isotope exchange (HIE) is most appealing because it allows fast and direct incorporation of D atoms at a late or the final stage of synthesizing the active pharmaceutical ingredient by replacing H with D, reducing the costs and time spent preparing intermediates or precursors for *de novo* syntheses. The state-of-the-art HIE strategies include: (i) homogeneous catalysis using transition metal complexes, such as [Ir],[8,9] [Co],[10] [Ni],[11] and [Fe];[12] (ii) heterogeneous catalysis using transition metals and their nanoparticles, such as Ru,[13] Rh,[7] and Pt;[14] and (iii) photoredox catalysis using molecular photocatalysts coupled with hydrogen atom transfer (HAT) catalysts (typically, thiols).[15,16] Transition-metal-complex-catalyzed HIE reactions typically target aromatic $C(sp^2)$–H sites. Heterogeneous catalysts such as Pd, Ru, Rh, Ir, and Pt can catalyze both $C(sp^2)$–H and $C(sp^3)$–H activation processes.[17] Photoredox protocols can efficiently and selectively install D at α-amino $C(sp^3)$–H bonds in a single step,[8,9] which is powerful because it can achieve high D incorporation. However, the current photocatalytic protocols are limited in labeling α- and β-$C(sp^3)$–H sites in tertiary amines.

The substrate scope of all existing HIE approaches is typically restricted to certain chemotypes and they cannot selectively label sites with similar chemical reactivity (Scheme 1A). The isotope-incorporation level also varies. Taking photocatalytic HIE of amines as an example:[15] photoexcitation of the photocatalyst generates an excited state to oxidize the amine to an amine radical cation, which then undergoes facile deprotonation at the α-$C(sp^3)$–H position to give an α-amino radical. At the same time, a deuterated thiol is generated *in situ* from the thiol HAT catalyst *via* H/D exchange with D_2O. Then, HAT between the deuterated thiol and α-amino radical results in a D-substituted amine and thiol radical. Electron transfer between the reduced photocatalyst and thiol radical regenerates the photocatalyst and deuterated thiol through protonation of the thiol anion. However, this protocol does not differentiate various α-amino $C(sp^3)$–H bonds (*e.g.*, all the α-amino sites of clomipramine are activated simultaneously, resulting in a high D incorporation of 7.22 D per molecule), so they are not suited for applications that require selective hydrogen labeling at a specific position. Therefore, methods that can label substrates with site-selective D incorporation (particularly among sites with similar chemical reactivity) are highly desirable.

Alternating current (AC) electrolysis provides an alternative way to sequentially perform redox-opposite reactions, like in a photoredox catalytic cycle, by periodically reversing the voltage polarity.[18–22] Unlike photoredox catalysis, AC electrolysis offers a facile way to tune the redox potentials and time duration of two redox events *via* voltage amplitude and AC frequency (f), enabling selective activation of sites with similar chemical reactivities. For example, we have previously shown that the electrochemical oxidation of tertiary amines to α-amino radicals takes place at an optimal substrate-dependent f.[23] At high f, the interconversion between an amine and its cationic radical is faster than the deprotonation of the cationic radical, so the formation of α-amino radicals is suppressed. However, at low f, the amine radical cation can be further oxidized to an iminium cation after deprotonation. Therefore, an optimal f is required to oxidize a tertiary amine to form its α-amino radical. Furthermore, because the deprotonation kinetics for amine substrates varies significantly, the optimal f differs by over two orders of

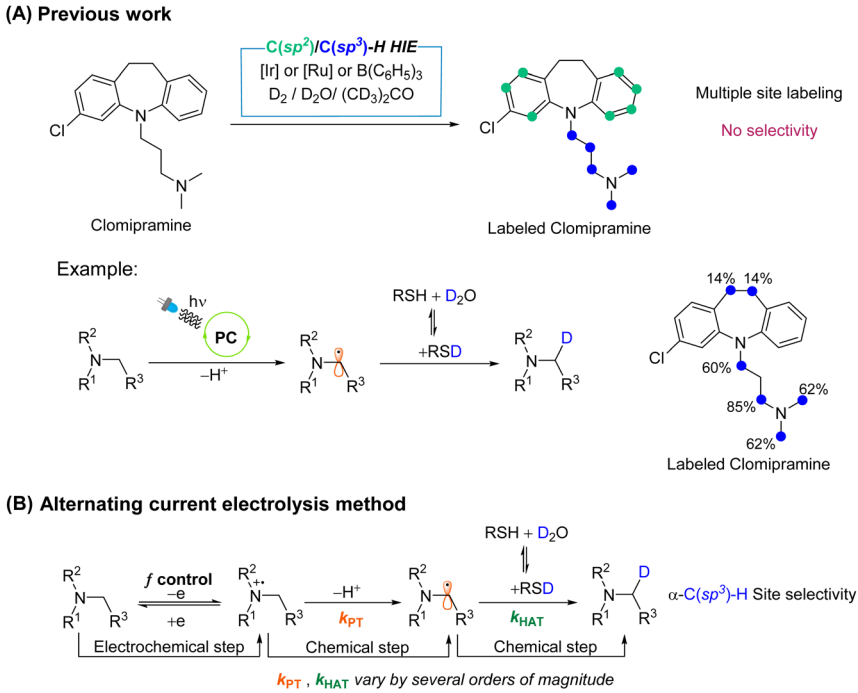

Scheme 1 Schematic illustration of (A) previously reported approaches for hydrogen isotope exchange (HIE) at C(sp^2)–H and C(sp^3)–H sites, highlighting the D-labelling of α-amine sites of clomipramine using a photocatalyst (PC) and HAT thiol catalyst as an example. (B) AC electrolysis method for deuteration at α-C(sp^3)–H sites that can potentially achieve α-amine site selectivity through AC-frequency (*f*)-controlled electrochemical and chemical (including PT and HAT) steps.

magnitude, providing a convenient handle to selectively activate α-amino C–H bonds in a molecule. AC electrolysis has also been found to affect the product selectivity of nickel-catalyzed cross-coupling reactions,[24] influence the chemoselectivity of carbonyl-compound and (hetero)arene reduction,[18,25] decrease the undesired reductive precipitation of metals,[26,27] and promote cross-coupling reactions such as formal C–O/O–H cross-metathesis.[28–30]

Inspired by these previous works, we hypothesize that selective HIE of amine sites can be achieved by their selective activation using an optimal AC frequency. Scheme 1B depicts our site-selective electrochemical HIE idea. The electrochemical HIE of amines includes three steps: (1) an amine substrate is electrochemically oxidized to its cation radical form, (2) the radical cation undergoes deprotonation to generate an amino radical in the presence of a base, and (3) HAT between the amino radical and deuterated thiol produces the D-labelled molecule. Because the rates of the last two chemical steps (*i.e.*, proton transfer (PT) and HAT) can vary by several orders of magnitude and depend on the bond dissociation energy (BDE) of the α-C(sp^3)–H bonds of the amine, we can control the time available for these two chemical steps by supplying different f values. More specifically, for amine sites with slow PT and HAT, the amine cation radical does not have time to be deprotonated and undergo HAT at high f (or with a short

anodic pulse) before it gets reduced back to its neutral molecular form. In contrast, amine sites with fast PT and HAT can finish the HIE even at high *f*, allowing site-selective HIE between amine sites with different PT and HAT kinetics using the AC frequency.

Results and discussion

In this study, we chose two tertiary amines with different α-amino sites, *N*-benzyltetrahydroisoquinoline (**1**) and *N*-(4-methoxyphenyl)pyrrolidine (**2**), as the model substrates to test our proposed site-selectivity idea in Scheme 1B. If our proposed idea is feasible, then the HIE of **1** and **2** should occur at two different *f* values. Fig. 1A illustrates our electrochemical HIE reaction design. We used methyl thioglycolate (MTG) as the HAT catalyst and precursor of the base for the deprotonation step and D_2O as the deuterium source. The amine substrate is first oxidized to generate an α-amino radical in the presence of the base during the positive pulse of the AC waveform. Then, the formed α-amino radical undergoes HAT with a deuterated thiol (RSD), which is *in situ* generated from the thiol and D_2O, to afford the deuterated amine and thiyl radical ($RS^{\bullet}$). Finally, $RS^{\bullet}$ is reduced back to the thiolate (RS^{-}) during the following negative voltage pulse, which acts as a base or is protonated to regenerate RSD, completing the HAT catalytic cycle. According to the reaction mechanism, oxidation of the amine and reduction of the thiol are required to drive the electrochemical HIE reaction of amines. We measured the redox potentials of **1**, **2**, and MTG using cyclic voltammetry. The cyclic voltammograms of **1** and **2** (Fig. 1B) show anodic peaks at 0.6 V and 0.2 V *vs.* Ag/Ag^{+}, respectively, assigned to single-electron oxidation of these amines to the

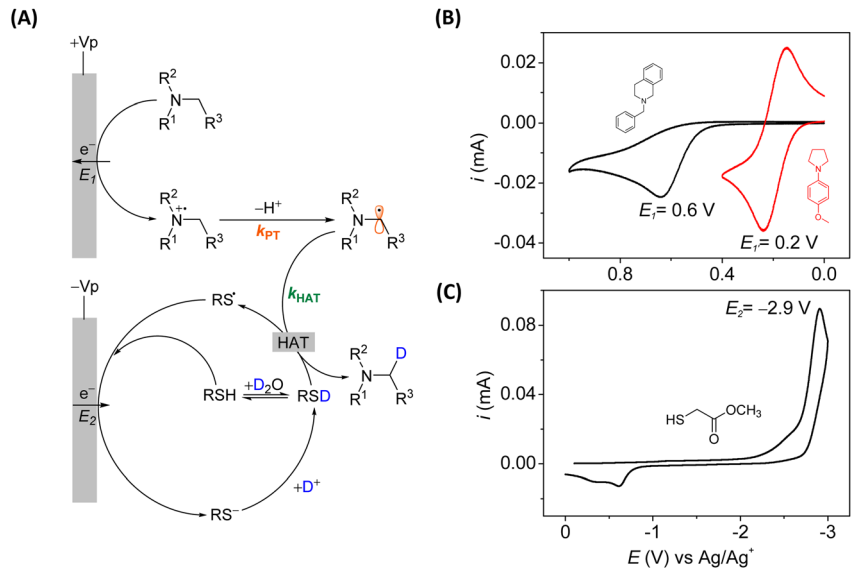

Fig. 1 (A) Proposed mechanism for AC-driven HIE of amines. Cyclic voltammograms of (B) **1** (black) and **2** (red) and (C) methyl thioglycolate (MTG) in *N*,*N*′-dimethylacetamide (DMA) containing 0.1 M $LiClO_4$. Scan rate: 0.1 V s^{-1}.

corresponding cation radicals.[23] The voltammogram of MTG (Fig. 1C) shows that electrochemical reduction of the thiol occurs at −2.9 V *vs.* Ag/Ag^+. Thus, we set the amplitudes of the AC waveform to be 3.5 V and 3.1 V after *iR* correction (see the ESI†) to drive the HIE reactions of **1** and **2**, respectively.

As previously discussed, the electrochemical HIE of amines comprises three steps: amine oxidation, PT, and HAT. We first measured the relative deprotonation kinetics (k_{PT}) using a voltammetric method (see the ESI†). Briefly, we varied the scan rate and compared the cyclic voltammograms of the amine with and without the base. At a low scan rate, the deprotonation step can be completed and consequently lead to overoxidation of the amine, resulting in a higher peak than the reference voltammogram without the base ($i_1 > i_0$). As the scan rate is increased, the available deprotonation time decreases, and the difference between i_0 and i_1 shrinks. Therefore, we can estimate the deprotonation time from the voltammograms where $i_1 \approx i_0$. For **1**, the deprotonation time is ~5 ms; for **2**, it is ~100 ms, giving a 20 : 1 ratio for the relative deprotonation kinetics. Note that the deprotonation only occurs at site **a** of **1** because of its weaker C–H bond than sites b and c.

Next, we estimated the relative HAT kinetics (k_{HAT}) from the calculated C–H BDE values for **1** and **2**. The BDE values for sites **a**, **b**, **c**, and **d** are 77, 82.3, 93, and 89.2 kcal mol^{-1}, respectively. Thus, the corresponding relative k_{HAT} ratios between sites a, b, c, and d are estimated to be $1 : 90 : 7 \times 10^5$ and $1 : 3 \times 10^4$, following the Evans–Polanyi correlation (see the ESI for calculation details†).[31] The k_{PT} and k_{HAT} values for **1** and **2** are summarized in Table 1. From the relative HAT and PT kinetics, we predict that the HIE at site a of **1** requires a much lower (by a few orders of magnitude) *f* than that at site d of **2** due to its small k_{HAT}.

To test our prediction, we conducted the HIE reactions of **1** and **2** using a sine waveform with different *f* values from 0 to 50 Hz (note: 0 Hz means DC electrolysis). For $f = 0$ Hz, we used two experimental setups: one home-built cell with an electrode–electrode distance (d) of 1 mm and one commercial IKA setup with $d = 5$ mm (see details in the Methods section). For other *f* values, we only used our home-built

Table 1 BDEs, oxidation potentials, and relative HAT and PT kinetics (k_{HAT} and k_{PT}) of **1** and **2**. BDE values were calculated using density functional theory (see Computational methods). The relative k_{HAT} was calculated from the BDE values.[31] The oxidation potential was obtained from the cyclic voltammograms in Fig. 1, and the relative k_{PT} (*for site a of **1**) was obtained from our previous report,[23] as discussed in the ESI†

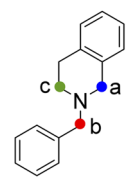

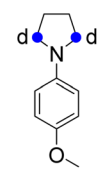

	1	**2**
BDE (kcal mol^{-1})	***a*** = 77.0, ***b*** = 82.3, ***c*** = 93.0	***d*** = 89.2
Relative HAT kinetics (k_{HAT})	***a*** : ***b*** : ***c*** = $1 : 90 : 7 \times 10^5$	***a*** : ***d*** = $1 : 3 \times 10^4$
Oxidation potential (V *vs.* Ag/Ag^+)	0.6	0.2
Relative deprotonation kinetics (k_{PT})	20*	1.0

setup. Table 2 shows the *f*-dependent D incorporation for **1** and **2**. At $f = 0$ Hz, we observed the highest D incorporation of 60% for **1** with the IKA setup and reduced D incorporation with our setup (40%). With increasing *f*, D incorporation dramatically decreases and then falls below the quantification limit of NMR (~7%), in agreement with the prediction that the slow HAT of **1** requires a long time or low *f* to be completed. In contrast, the highest D incorporation of 89% for **2** was observed at $f =$ 0.5 Hz. However, at $f = 0$ Hz, D incorporation plummets to only <8% and 16% using the IKA setup and our setup, respectively. D incorporation slightly decreased to ~80% at $f > 0.5$ Hz. The high D incorporation observed in **2** at high *f* is also consistent with our prediction. However, the low D incorporation at $f = 0$ Hz is not predicted by the proposed reaction scheme in Scheme 1B because the fast chemical steps (PT + HAT) should not prevent HIE from happening at low *f*.

The different *f*-dependent D-incorporation values for **1** and **2** encouraged us to conduct a detailed analysis of the products to understand the electrochemical HIE reaction mechanism. Fig. 2A and C show the product distribution in terms of starting material (SM) conversion during the electrochemical HIE reactions of **1** and **2**, respectively, at different *f* values. Note that here we assigned an equivalent *f* for the DC electrolysis condition, considering that when the substrate or intermediates diffuse between the anode and cathode, they will experience an opposite redox environment, just like during the AC electrolysis. Therefore, we calculated the equivalent AC frequency from the diffusion time between the two electrodes in the electrolytic cell (for example, 3.5×10^{-5} Hz for the IKA setup and 8.7×10^{-4} Hz for our homebuilt setup for **1**; see the ESI for calculation details†). Also, the deuterated SM (*i.e.*, the desired product) and SM cannot be separated, so they were plotted as a group in the product distribution analysis. For the HIE of **1**, we observed significantly increased formation of dimers of **1** (from 0 to 40%) accompanied by a dramatic decrease in the D incorporation (from ~60% to <10%, as shown in Fig. 2B) as *f* increased from $\sim 10^{-5}$ to $\sim 10^{1}$ Hz. The formation of dimers indicates the successful deprotonation of the amine cation radicals to α-amino radicals, and the low D incorporation indicates that the HAT step in this

Table 2 AC frequency-dependent D incorporation during HIE of **1** and **2**. The applied voltage amplitudes for **1** (0.3 equiv. MTG) and **2** (0.8 equiv. MTG) are 3.5 and 3.1 V, respectively

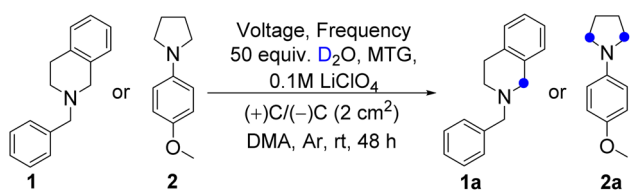

f (Hz)	**1a**	**2a**
0.00	60% (IKA), 40% (our setup)	<8% (IKA), 16% (our setup)
0.05	13%	78%
0.50	<6%	89%
10.0	<7%	78%
50.0	<7%	80%

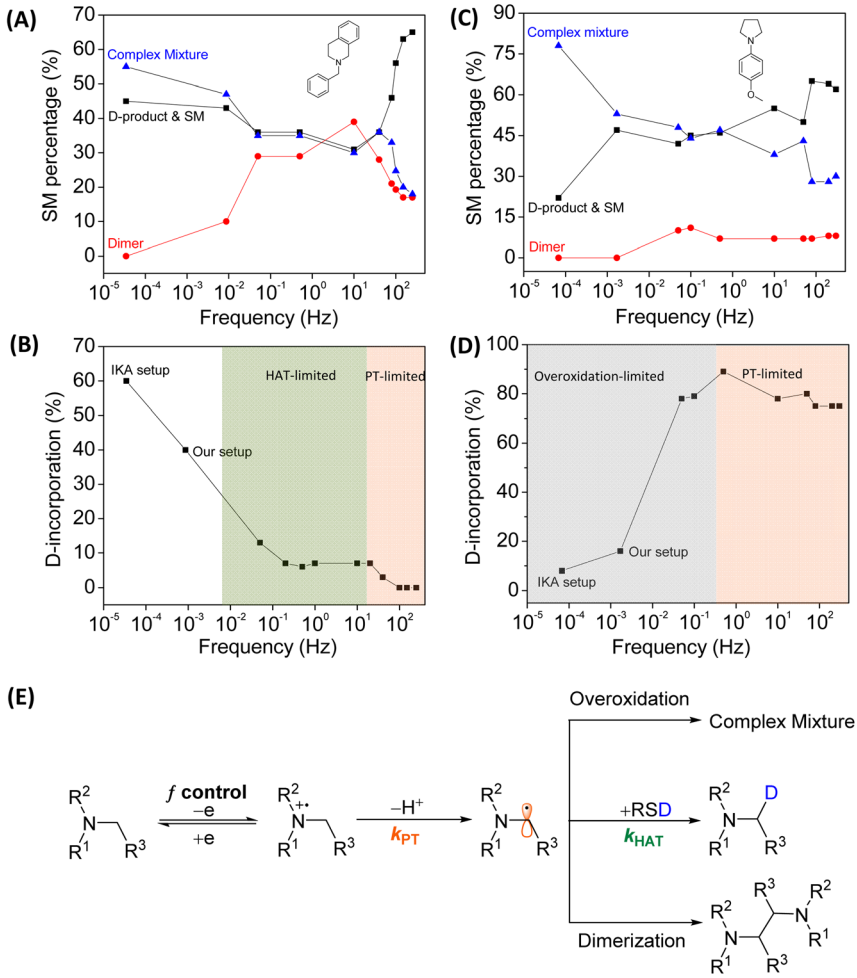

Fig. 2 *f*-dependence of product distribution in terms of starting material (SM) conversion and D incorporation for **1** (A and B) and **2** (C and D). (E) Illustration of the *f*-controlled pathways towards forming the D-substituted amine, dimer, and overoxidized complex mixture.

frequency range limits the HIE reaction. More quantitatively, the D incorporation reaches a plateau value of ~7% at $f = \sim 0.1$ Hz, suggesting that the HAT between the deuterated thiol and α-amino radical typically requires a time (t_{HAT}) longer than ~10 s. As f increases beyond 20 Hz, the D incorporation decreases to zero, the dimer formation is suppressed, and the SM is recovered (~60%), suggesting that the deprotonation step is now the limiting factor due to the conversion of the amine cation radical back to the SM. Therefore, we can estimate the deprotonation time (t_{PT}) to be on the order of ~0.05 s.

In comparison, for the HIE of **2**, the highest D incorporation of 89% was achieved at 0.5 Hz (Fig. 2D). The D incorporation decreases drastically at frequencies <0.5 Hz and under DC conditions, accompanied by low SM and deuterated-product yields and significant formation of a complex mixture due to overoxidation. For

example, DC electrolysis using an IKA setup resulted in ~10% D incorporation, ~20% yield of the SM and deuterated product, and >75% yield of overoxidized products, indicating that the HIE is limited by the overoxidation reactions. At $f >$ 0.5 Hz, the D incorporation slightly decreases, but the yield of the SM and deuterated product increases, similar to what happened for the HIE of **1** at $f >$ ~20 Hz (Fig. 2B). Such opposite correlation between D incorporation and SM/D-product yield is an indicator of a PT-limited process. Similarly, we can estimate t_{PT} for **2** to be ~2 s. The dimer formation is insignificant (<15%) over the entire frequency range, and efficient D incorporation was observed even at f as high as 300 Hz, suggesting that the typical t_{HAT} should be shorter than 0.003 s (estimated from the highest experimentally tested f of 300 Hz). Table 3 summarizes the estimated t_{PT} and t_{HAT} for **1** and **2** from the f-dependent product and D-incorporation analysis in Fig. 2 and the predicted relative t_{PT} and t_{HAT} from Table 1, revealing a quantitative agreement between the experimentally determined values and predicted ones.

From the analysis above, we found that (1) efficient HAT and low overoxidation were critical to achieving high D incorporation, and (2) slow deprotonation had some adverse but not critical effects on the final D incorporation. These findings suggest that the competition between the different reaction pathways of α-amino radicals (HAT, dimerization, and overoxidation) is the key factor in determining the D-incorporation efficiency (Fig. 2E). For **1**, under any AC conditions, the dimerization of α-amino radicals outcompetes HAT, resulting in low D incorporation. Under DC conditions, dimerization is insignificant because the concentration of α-amino radicals decreases due to concentration polarization (the amine substrate is depleted near the electrode surface under a constant potential, thus lowering the radical concentration). Therefore, the α-amino radicals have enough time to complete HAT, which is a slow process for **1**. However, for **2**, at $f <$ 0.5 Hz, the overoxidation of α-amino radicals dominates, leading to low D incorporation and yield. This is not surprising because α-amino radicals of pyrrolidine can easily undergo overoxidation to form iminium cations or further oxidized products in an oxidizing environment in the presence of a base.[23] At high f, the slow deprotonation does affect the availability of α-amino radicals due to the reverse reaction of amine cation radicals to the amine. However, due to the highly efficient HAT, α-amino radicals are effectively deuterated whenever available. Therefore, the final D incorporation remains relatively high at high f as long as the reaction time is sufficient.

Guided by our findings using **1** and **2** as the model substrates, we continued to determine the optimal conditions for the HIE of various tetrahydroisoquinolines, pyrrolidines, and a piperidine (**3–24**). We calculated their BDEs and predicted their relative k_{HAT}. Fig. 3A and B show that the k_{HAT} values for *N*-aryl tetrahydroisoquinoline substrates **3–13** and pyrrolidine/piperidine substrates **14–24** are comparable to those of **1** and **2**, respectively. The slow HAT kinetics of

Table 3 Estimated time scale for deprotonation (t_{PT}) and HAT (t_{HAT}) for **1** and **2**

	t_{PT}	t_{HAT}
1	~0.05 s	$\gtrsim$10 s
2	~2 s	<0.003 s
Experimental $t(\mathbf{1})/t(\mathbf{2})$	~40 : 1	$>3 \times 10^3 : 1$
Predicted $t(\mathbf{1})/t(\mathbf{2})$	20 : 1	$3 \times 10^4 : 1$

tetrahydroisoquinoline substrates requires performing the HIE reaction under DC conditions. In contrast, HAT should not be the limiting step for the HIE reaction of pyrrolidine/piperidine substrates. The limiting factor should be the undesired overoxidation of α-amino radicals, which can be reduced by increasing *f*. Thus, we adopted $f = 0.5$ Hz considering the similarity between **2** and the other pyrrolidine/piperidine substrates in terms of their BDEs, unless the D incorporation was not satisfactory, in which case we further increased *f*.

Fig. 4 shows the substrate scope. Tetrahydroisoquinolines with *N*-aryl rings bearing electron-donating groups such as methoxy, methyl, tertiary butyl, dimethyl, phenyl and dioxane (**3–9**) and electron-withdrawing substituents such as fluoro and trifluoromethyl (**10–13**) worked well under DC conditions affording high D incorporation of 70–93%. During the substrate-scope development, we varied the reaction time for different *N*-aryl tetrahydroisoquinoline substrates between 15 and 48 h to improve the yield under the DC electrolysis conditions. However, due to the overoxidation of the benzylic position in *N*-aryl tetrahydroisoquinolines, the yield for the deuterated products is still limited (~10–60%). On the other hand, *N*-aryl pyrrolidines bearing electron-donating groups such as methyl, tertiary butyl, phenyl, dioxane, ethyl acetate, and ethanol (**14**, **16–21**) afforded a moderate to good D incorporation of 52–89% at 0.5 Hz. Due to the steric hindrance, methyl groups at the *ortho* position of the *N*-aryl ring (**15**) led to low D incorporation of 36%. The *N*-aryl pyrrolidines substituted with electron-withdrawing groups such as Cl and Br (**22** and **23**) resulted in less D incorporation (23 and 36%) at 0.5 Hz, possibly due to a dehalogenation reaction. In the case of *N*-aryl piperidine with a methoxy group on the ring (**24**), we observed poor D incorporation (23%) and low yield (42%) at 0.5 Hz but significantly improved D incorporation of 50% and better yield of 51% at 50 Hz. The improvement at higher *f* is because the impaired overlap between the lone pair of the amine and the unpaired electron at the α-carbon significantly destabilizes the α-amino radical intermediate, leading to fast overoxidation kinetics that requires high *f* to suppress the overoxidation. How to quantitively determine the

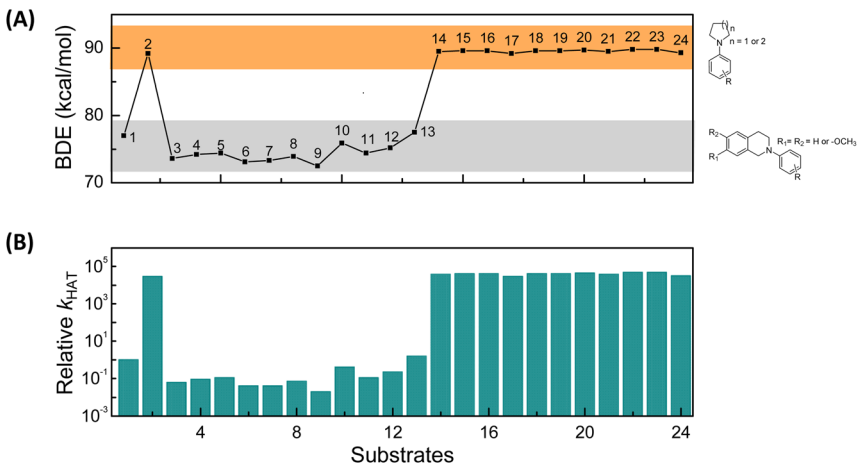

Fig. 3 (A) Calculated BDE values and (B) predicted relative HAT rates at α-amino C(sp^3)–H sites for different substituted tetrahydroisoquinolines (**1**, **3–13**) and pyrrolidines (**2**, **14–23**) and a piperidine (**24**).

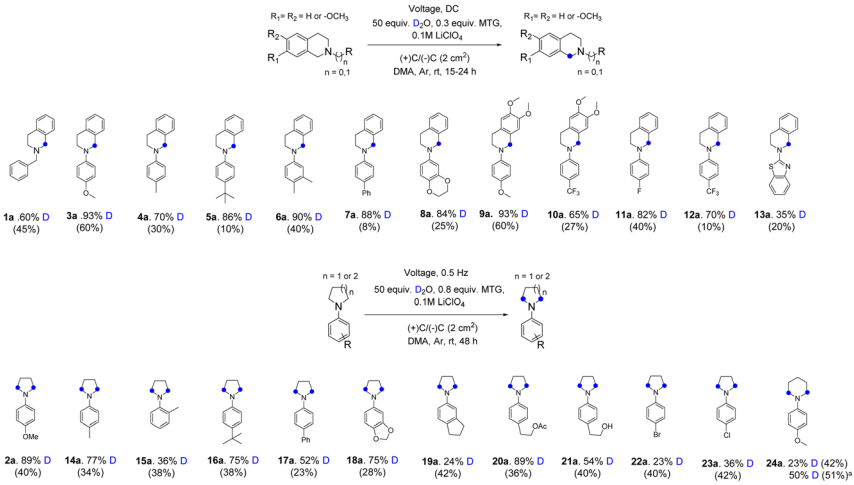

Fig. 4 Substrate scope of the electrochemical HIE reaction. [a]Reaction was conducted at 50 Hz. D incorporation was determined by ^{1}H NMR peak integration relative to an unlabeled compound. All isolated yields are provided in parentheses. The experimental voltage for each substrate is provided in the ESI.†

overoxidation kinetics for predicting the optimal f of HIE reactions for different types of amine substrates is still being studied.

Conclusions

In conclusion, we reported an electrochemical protocol for the HIE of α-amino C(sp^3)–H bonds for the first time. Tetrahydroisoquinolines and pyrrolidines were selected as the two categories of model substrates in this study. We achieved the best D incorporation at $f = 0$ Hz (*i.e.*, DC electrolysis conditions) for tetrahydroisoquinolines and at 0.5 Hz for pyrrolidines. The two different optimal HIE frequencies arise from their different PT and HAT kinetics. Because the HAT rate of tetrahydroisoquinolines is four orders of magnitude slower than that of the pyrrolidines, the HIE of tetrahydroisoquinolines requires DC conditions, under which the dimerization pathway is suppressed, and HAT has sufficient time to be completed. For pyrrolidines, the high HAT rate allows the HIE to occur at high f, but the overoxidation of its α-amino radical intermediates outcompetes the HAT at low f, resulting in low D incorporation and low yield. The AC-frequency-dependent HIE for different amines can be utilized for selective isotope labeling of α-amino C(sp^3)–H sites in one drug molecule, which will be significant and advantageous to the pharmaceutical industry.

Methods

Chemicals and materials

Tertiary amines were synthesized following the protocol in the ESI.† $LiClO_4$ (>95%, MilliporeSigma), methyl thioglycolate (MTG, 95%, MilliporeSigma), D_2O (99 atom% D, MilliporeSigma) and *N*,*N*′-dimethylacetamide (DMA) (anhydrous, 99.8%, MilliporeSigma) were used as received.

Experimental setups for electrochemical HIE reactions

IKA setup. The IKA ElectraSyn 2.0 purchased from IKA has a reaction vial, vial cap, graphite electrodes, electrode holder, and base unit with a stirrer and vial holder (Fig. S1†). Both graphite electrodes (3 mm in thickness, ~1 cm in width, and ~5 cm in length) are attached to the vial cap with an electrode–electrode separation of ~5 mm and inserted in a vial containing the reaction mixture in 4 mL DMA. The vial is connected to a power supply through the vial holder. Then the output voltage and time can be applied as per the reaction conditions.

Our setup. In this setup, a waveform generator, amplifier, two glassy carbon plate electrodes (3 mm in thickness, 1 cm in width, and ~10 cm in length) and a Schlenk tube were used for the HIE reaction (Fig. S2†). The electrodes were inserted into the reaction flask with an electrode–electrode separation of ~1 mm in 4 mL of DMA and partially immersed (~2 cm) in the solution. Then the electrodes were connected to a waveform generator linked to the amplifier by applying the output voltage and frequency.

General procedures for DC and AC electrolysis

DC electrolysis. An oven-dried 5 mL ElectraSyn reaction vial containing a magnetic stir bar was charged with tertiary amine (0.25 mmol, 1.0 equiv.), $LiClO_4$ (0.5 mmol, 2.0 equiv.), MTG (0.15 mmol, 0.3 equiv.), D_2O (12.5 mmol, 50 equiv.) and anhydrous DMA (4.0 mL) under an argon atmosphere. Using two graphite electrodes, the reaction mixture was electrolyzed at a constant voltage of 3.2 to 3.9 V for 15–24 hours. After completion of the reaction, the electrodes were removed, and the reaction mixture was diluted with ethyl acetate (10 mL). The organic layer was washed with a saturated $NaHCO_3$ solution (15 mL) and brine (saturated NaCl, 15 mL). The separated organic layer was dried over Na_2SO_4 and concentrated under reduced pressure. The crude product was purified using flash silica-gel chromatography with ethyl acetate and hexane to afford the desired products.

AC electrolysis. An oven-dried 10 mL Schlenk tube containing a triangular magnetic stir bar was charged with tertiary amine (0.25 mmol, 1.0 equiv.), $LiClO_4$ (0.5 mmol, 2.0 equiv.), MTG (0.2 mmol, 0.8 equiv.), D_2O (12.5 mmol, 50.0 equiv.), and anhydrous DMA (4.0 mL) under an argon atmosphere. Two glassy carbon plate electrodes were then inserted into the reaction flask and connected to a waveform generator linked to the amplifier. The output voltage and frequency were set to 3–4 V and 0–300 Hz, and the reaction mixture was allowed to stir at room temperature for 48 h. Then, the electrodes were removed, and the reaction mixture was diluted with ethyl acetate (10 mL). The organic layer was washed with brine (15 mL), and the separated organic layer was dried over Na_2SO_4 and then concentrated under reduced pressure. The crude product was purified using flash silica-gel chromatography with ethyl acetate and hexane to afford the desired products.

Cyclic voltammetry. All cyclic voltammograms were collected using a Schlenk tube fitted with a 3 mm-diameter glassy carbon disk electrode as the working electrode, a glassy carbon plate as the counter electrode, and an Ag/Ag^+ electrode as the reference electrode under an argon atmosphere. The Ag/Ag^+ electrode was prepared by filling the glass tube with 10 mM $AgNO_3$ and $LiClO_4$ (0.1 M, supporting electrolyte) in an anhydrous DMA solution. The Ag/Ag^+

reference electrode potential was calibrated using ferrocene/ferrocenium ($E_{Fc/Fc^+} = 0.11$ *vs.* Ag/Ag^+) (Fig. S3†). The glassy carbon disk electrode was cleaned by polishing with a series of alumina powders (0.3 and 0.05 μm) and then sonicated and washed with a large amount of deionized water and methanol before use. All the electrodes were dried in air before the electrochemical measurements.

NMR analysis for H/D exchange quantification. D incorporation was quantified by the decrease in ^{1}H NMR integral intensities at the specified positions compared to the unlabeled starting material.

Computational methods. We computed the α-C(sp^3)–H BDEs using spin-polarized density functional theory as implemented in the Quantum Espresso Package.[32] The calculations employed the projector augmented wave method[33] and the Perdew–Burke–Ernzerhof functional.[34] The neutral molecules and their radicals generated from homolytic cleavage of the C–H bonds at the benzylic and α-amine positions were fully optimized in a sufficiently large box of 30 × 30 × 30 Å using an energy cutoff of 50 Ry and Γ-point sampling until the Hellmann–Feynman forces were less than 0.04 eV $Å^{-1}$, after which their total energies were computed. The hydrogen BDEs were defined as:

$$\mathrm{BDE} = E(\mathrm{R}^{\bullet}) + E(\mathrm{H}^{\bullet}) - E(\mathrm{R\text{–}H}),$$

where R–H is the neutral molecule, $R^{\bullet}$ is the radical after the cleavage of the C–H bond, and $H^{\bullet}$ is the hydrogen radical.

Author contributions

The manuscript was written through the contributions of all authors. All authors have given approval to the final version of the manuscript. JF and ZL performed the theoretical calculations.

Conflicts of interest

There are no conflicts to declare.

Acknowledgements

NB, DG, JM, and LL gratefully acknowledge support from the NIH (1R35 GM142590-01), start-up funds, a Rumble Fellowship, and a Faculty Competition for Postdoctoral Fellows award from Wayne State University. The computational part of this work was supported by the U.S. Department of Energy (DOE), Office of Science, Basic Energy Sciences, under award no. DE-SC0023324, and used resources of the National Energy Research Scientific Computing Center (NERSC), a DOE Office of Science User Facility supported by the Office of Science of the U.S. DOE under contract no. DE-AC02-05CH11231 using NERSC award BES-ERCAP0023653. JF acknowledges a Rumble Fellowship and the A. Paul and Carole C. Schaap Endowed Distinguished Graduate Award in Chemistry from Wayne State University. The authors also acknowledge the valuable feedback from Dr Jingwei Li and Zheng Huang of Merck & Co.

References

1 J. Atzrodt and V. Derdau, *J. Labelled Compd. Radiopharm.*, 2010, **53**, 674–685.
2 D. H. Chace, T. Lim, C. R. Hansen, B. W. Adam and W. H. Hannon, *Clin. Chim. Acta*, 2009, **402**, 14–18.
3 A. Nakanishi, Y. Fukushima, N. Miyazawa, K. Yoshikawa, T. Maeda and Y. Kurobayashi, *J. Agric. Food Chem.*, 2017, **65**, 5026–5033.
4 N. Penner, L. Xu and C. Prakash, *Chem. Res. Toxicol.*, 2012, **25**, 513–531.
5 T. Pirali, M. Serafini, S. Cargnin and A. A. Genazzani, *J. Med. Chem.*, 2019, **62**, 5276–5297.
6 T. G. Gant, *J. Med. Chem.*, 2014, **57**, 3595–3611.
7 E. Levernier, K. Tatoueix, S. Garcia-Argote, V. Pfeifer, R. Kiesling, E. Gravel, S. Feuillastre and G. Pieters, *JACS Au*, 2022, **2**, 801–808.
8 W. J. Kerr, G. J. Knox and L. C. Paterson, *J. Labelled Compd. Radiopharm.*, 2020, **63**, 281–295.
9 M. Daniel-Bertrand, S. Garcia-Argote, A. Palazzolo, I. Mustieles Marin, P.-F. Fazzini, S. Tricard, B. Chaudret, V. Derdau, S. Feuillastre and G. Pieters, *Angew. Chem., Int. Ed.*, 2020, **59**, 21114–21120.
10 W. N. Palmer and P. J. Chirik, *ACS Catal.*, 2017, **7**, 5674–5678.
11 H. Yang, C. Zarate, W. N. Palmer, N. Rivera, D. Hesk and P. J. Chirik, *ACS Catal.*, 2018, **8**, 10210–10218.
12 R. Pony Yu, D. Hesk, N. Rivera, I. Pelczer and P. J. Chirik, *Nature*, 2016, **529**, 195–199.
13 C. Taglang, L. M. Martínez-Prieto, I. del Rosal, L. Maron, R. Poteau, K. Philippot, B. Chaudret, S. Perato, A. Sam Lone, C. Puente, C. Dugave, B. Rousseau and G. Pieters, *Angew. Chem., Int. Ed.*, 2015, **54**, 10474–10477.
14 H. Sajiki, N. Ito, H. Esaki, T. Maesawa, T. Maegawa and K. Hirota, *Tetrahedron Lett.*, 2005, **46**, 6995–6998.
15 Y. Y. Loh, K. Nagao, A. J. Hoover, D. Hesk, N. R. Rivera, S. L. Colletti, I. W. Davies and D. W. C. MacMillan, *Science*, 2017, **358**, 1182–1187.
16 Q. Shi, M. Xu, R. Chang, D. Ramanathan, B. Peñin, I. Funes-Ardoiz and J. Ye, *Nat. Commun.*, 2022, **13**, 4453.
17 M. Lepron, M. Daniel-Bertrand, G. Mencia, B. Chaudret, S. Feuillastre and G. Pieters, *Acc. Chem. Res.*, 2021, **54**, 1465–1480.
18 K. Hayashi, J. Griffin, K. C. Harper, Y. Kawamata and P. S. Baran, *J. Am. Chem. Soc.*, 2022, **144**, 5762–5768.
19 J. Fährmann and G. Hilt, *Angew. Chem., Int. Ed.*, 2021, **60**, 20313–20317.
20 S. Rodrigo, D. Gunasekera, J. P. Mahajan and L. Luo, *Curr. Opin. Electrochem.*, 2021, **28**, 100712.
21 N. E. Tay, D. Lehnherr and T. Rovis, *Chem. Rev.*, 2022, **122**, 2487–2649.
22 J. Zhong, C. Ding, H. Kim, T. McCallum and K. Ye, *Green Synthesis and Catalysis*, 2022, **3**, 4–10.
23 D. Gunasekera, J. P. Mahajan, Y. Wanzi, S. Rodrigo, W. Liu, T. Tan and L. Luo, *J. Am. Chem. Soc.*, 2022, **144**, 9874–9882.
24 E. O. Bortnikov and S. N. Semenov, *J. Org. Chem.*, 2021, **86**, 782–793.
25 Y. Kawamata, K. Hayashi, E. Carlson, S. Shaji, D. Waldmann, B. J. Simmons, J. T. Edwards, C. W. Zapf, M. Saito and P. S. Baran, *J. Am. Chem. Soc.*, 2021, **143**, 16580–16588.

26 C. Schotten, C. J. Taylor, R. A. Bourne, T. W. Chamberlain, B. N. Nguyen, N. Kapur and C. E. Willans, *React. Chem. Eng.*, 2021, **6**, 147–151.
27 L. Zeng, Y. Jiao, W. Yan, Y. Wu, S. Wang, P. Wang, D. Wang, Q. Yang, J. Wang and H. Zhang, *Nat., Synth.*, 2023, 1–10.
28 D. Wang, T. Jiang, H. Wan, Z. Chen, J. Qi, A. Yang, Z. Huang, Y. Yuan and A. Lei, *Angew. Chem., Int. Ed.*, 2022, **61**, e202201543.
29 Y. Yuan, J.-C. Qi, D.-X. Wang, Z. Chen, H. Wan, J.-Y. Zhu, H. Yi, A. D. Chowdhury and A. Lei, *CCS Chem.*, 2022, **4**, 2674–2685.
30 E. O. Bortnikov, B. S. Smith, D. M. Volochnyuk and S. N. Semenov, *Chem. – Eur. J.*, 2023, **29**, e2022038.
31 J. M. Mayer, *Acc. Chem. Res.*, 2011, **44**, 36–46.
32 P. Giannozzi, O. Andreussi, T. Brumme, O. Bunau, M. Buongiorno Nardelli, M. Calandra, R. Car, C. Cavazzoni, D. Ceresoli, M. Cococcioni, N. Colonna, I. Carnimeo, A. Dal Corso, S. de Gironcoli, P. Delugas, R. A. DiStasio, A. Ferretti, A. Floris, G. Fratesi, G. Fugallo, R. Gebauer, U. Gerstmann, F. Giustino, T. Gorni, J. Jia, M. Kawamura, H. Y. Ko, A. Kokalj, E. Küçükbenli, M. Lazzeri, M. Marsili, N. Marzari, F. Mauri, N. L. Nguyen, H. V. Nguyen, A. Otero-de-la-Roza, L. Paulatto, S. Poncé, D. Rocca, R. Sabatini, B. Santra, M. Schlipf, A. P. Seitsonen, A. Smogunov, I. Timrov, T. Thonhauser, P. Umari, N. Vast, X. Wu and S. Baroni, *J. Phys.: Condens. Matter*, 2017, **29**, 465901.
33 P. E. Blöchl, *Phys. Rev. B: Condens. Matter Mater. Phys.*, 1994, **50**, 17953.
34 J. P. Perdew, K. Burke and M. Ernzerhof, *Phys. Rev. Lett.*, 1996, 77, 3865.

